



A nanoscale mechanism of hydrogen embrittlement in metals

Jun Song^{*}, W.A. Curtin

School of Engineering, Brown University, Providence, RI 02912, USA

Received 9 July 2010; received in revised form 4 November 2010; accepted 7 November 2010

Available online 13 December 2010

Abstract

The embrittlement of metallic systems by hydrogen is a widespread phenomenon but the precise role of hydrogen in this process is not well understood and predictive mechanisms are not available. Here, a new model is proposed wherein hydrogen accumulation around a microcrack tip prevents crack-tip dislocation emission or absorption, and thus suppresses crack-tip blunting and ductile fracture while promoting cleavage fracture. The conceptual model is demonstrated via atomistic simulations of the evolution of equilibrium hydrogen distributions around a crack tip in Ni under increasing applied load, followed by measurement of dislocation emission and/or cleavage. These analyses are performed in single crystal Ni and for several tilt grain boundaries and several initial crack notch radii, using molecular statics and embedded-atom-method interatomic potentials. A kinetic analysis is used to calculate the size of the “nanohydride” formed at the crack tip as a function of hydrogen chemical potential, temperature, H diffusion rate, load level, and loading rate. Combining the kinetic analysis with the deformation/fracture analysis generates a mechanism map that predicts a ductile-to-brittle transition as a function of material and loading parameters. The mechanism map is applied to predict H embrittlement of unnotched tensile specimens of Ni, and the predictions and experiments match well for material parameter values expected to be pertinent in these materials. The mechanism proposed and validated here directly identifies the role of H in driving a change in fracture mode and toughness as a function of material and loading parameters.

© 2010 Acta Materialia Inc. Published by Elsevier Ltd. All rights reserved.

Keywords: Hydrogen embrittlement; Fracture; Dislocation; Diffusion; Ductility

1. Introduction

The ingress of H into metals leads to a variety of processes that makes materials more prone to failures. In metallic systems such as high strength steels and nickel, the presence of H often embrittles the material by causing a sharp transition from ductile fracture (i.e. microvoid coalescence) to brittle intergranular fracture accompanied by a drastic loss in toughness and ductility [1–6], although substantial plastic deformation may still occur. For instance, plastic deformation (e.g. slip traces) along the fracture path is observed when embrittlement occurs in Ni and its alloys [2–4,7]. Extensive experimental and theoretical studies have led to a number of proposed mechanisms for hydrogen embrittlement. The main competing models are hydrogen-enhanced decohesion

(HEDE) [8–13], hydrogen-enhanced local plasticity (HELP) [14–16], and hydride formation and cleavage [17–19]. In the HEDE mechanism, the presence of H atoms is assumed to lower the surface energy of atomic planes or grain boundaries, encouraging more cleavage-like failure as suggested by the Griffith criterion for brittle fracture. This mechanism is supported by some experiments [13,20,21] showing good correlation between the measured cleavage toughness and H concentration. However, in those experiments brittleness and plasticity coexist [22] so that direct quantification of the decohesion effect is not available. In the HELP mechanism, H is envisioned to form Cottrell atmospheres [23] around dislocation cores which may facilitate dislocation motion or decrease dislocation–dislocation interactions, leading to an increase in local plasticity and subsequent failure by exhaustion of the material plastic strain capacity or failure from cracks nucleated by dislocation pile-ups. The HELP mechanism is supported primarily by experimental

^{*} Corresponding author. Tel.: +1 401 863 1477.
E-mail address: Jun_Song@Brown.edu (J. Song).

observations of enhanced dislocation motion [24–26] and localized slip bands in the vicinity of the crack tip in H-charged test specimens [27,28]. The HELP mechanisms are also in accordance with some studies [29–32] where the material yield stress is reduced in the presence of H which, near a crack tip, could lead to softening and localization phenomena. The HELP mechanism is expected to occur over a wide range of hydrogen concentration and can account for the localized deformation within a region of several hundred nanometers from the fracture surface [24,29]. However, the actual process of embrittlement at the crack tip is difficult to determine, while increases in flow stress in the presence of H are also observed in various materials [33–38]. Finally, hydride formation and cleavage is a viable embrittlement mechanism when brittle hydride precipitates form [39–42], but is only expected in “hydride-forming” systems such as V and Nb, although limited hydride formation can be observed in other materials (e.g. Ni) [7,33] undergoing hydrogen embrittlement.

Complementing the experiments above, modeling and simulation work has been carried out to examine the various proposed H embrittlement mechanisms. The thermodynamic framework for segregation of H and consequent modifications to the fracture energy are well-recognized, supporting the HEDE concept [43,44]. However, simulations that directly examine the H influence on the fracture energy can also show only modest effects on decohesion in some materials such as Ni, where H embrittlement is observed experimentally [45–47]. Stress-driven H migration and its effects on microstructure evolution or possible hydride formation at the crack tip have been investigated via continuum modeling [48–50]. However, high bulk H concentrations far beyond those commonly attained in experiments were used. In addition, the complex interactions between H and lattice defects at the nanoscale are not well accounted for, while it has been shown in other studies [51–54] that those interactions are critical, especially in the initial stage of the H embrittlement.

Overall, while each mechanism has distinct merits, and while different mechanisms may operate in different materials, quantifiable predictions based on fundamental mechanisms have not yet clearly emerged. The field is thus open for more in-depth analysis, experiments, and mechanisms.

Here we propose a mechanism for H embrittlement that is a nanoscale analogy to hydride formation but is not restricted to strong hydride formers, and that has elements of the HEDE model, but is distinct in its prediction of a ductile-to-brittle transition that can be related to key material properties. Specifically, we propose that diffusion of H to a crack tip leads to a very high local H concentration that corresponds, essentially, to the formation of a “nanohydride” material. The key feature of this “nanohydride” material (e.g. H concentrations approaching those of the accepted bulk hydride phase) is its ability to prevent dislocation emission or absorption at the crack tip, thereby suppressing blunting of cracks, inhibiting ductile fracture mechanisms, and driving cleavage failure. The formation

of this “nanohydride” is consistent with some experimental observations that suggest very high H concentrations in the immediate vicinity of the crack tip [55,56].

We envision the above mechanism as operating on pre-existing microcracks in a material, which are normally blunted by crack-tip emission or plasticity, and leading to brittle-like failure although with surrounding bulk plasticity in the material. Nucleation and growth of microcracks can play important roles in metal failure [57–59]. A schematic of the process is shown in Fig. 1. Fig. 1a shows a microcrack that, in the absence of hydrogen, emits and/or absorbs dislocations and becomes blunted. Such a microcrack cannot propagate and plays no significant role in fracture. Fig. 1b shows that, in the presence of sufficient hydrogen and hydrogen diffusion rate, the microcrack tip can have a different history. Specifically, H can accumulate in the immediate vicinity of the crack tip due to the crack-tip stress fields, similar to larger-scale models [45,49,60]. If sufficient H can accumulate fast enough, relative to the applied loading rate, then dislocation emission and absorption at the crack tip can be suppressed and the hydride-like material can undergo cleavage. Once cleaved, the hydride can quickly reform by short-range diffusion to re-develop the brittle material ahead of the crack tip and continue the brittle fracture process. Deformation around the microcrack(s) due to the usual plasticity still exists and contributes to toughness but the fracture mode is changed from ductile-like void nucleation and growth, with large energy dissipation, to cleavage-like fracture with some bulk plastic dissipation.

The remainder of this paper is aimed at explicitly demonstrating the operation of the phenomenon sketched above through atomistic modeling in the Ni–H system, development of a mechanism map that includes the kinetics of H diffusion to the crack tip, and then exercising the model for the Ni–H system. In Section 2 we describe the computational methodology. In Section 3.1 we present the results of “nanohydride” formation, inhibition of dislocation nucleation, and nanohydride cleavage fracture. In Section 3.2–3.3 we develop a kinetic model for H transport that controls the rate of “nanohydride” formation, and present a comprehensive mechanism map for embrittlement. In Section 3.4 we apply the overall model to predict the regime of embrittlement in Ni–H at room temperature. In Section 4 we discuss our model further in the context of the existing literature.

2. Computation methodologies

2.1. Atomistic modeling

We aim to model the fracture and dislocation emission behavior at the tip of a microcrack, which necessitates an atomistic description. To accommodate both dislocation emission and expansion of material as H accumulates, we use the finite-temperature coupled atomistic/discrete-dislocation (CADD) multiscale method, which consists of a fully atomistic region around the crack tip surrounded

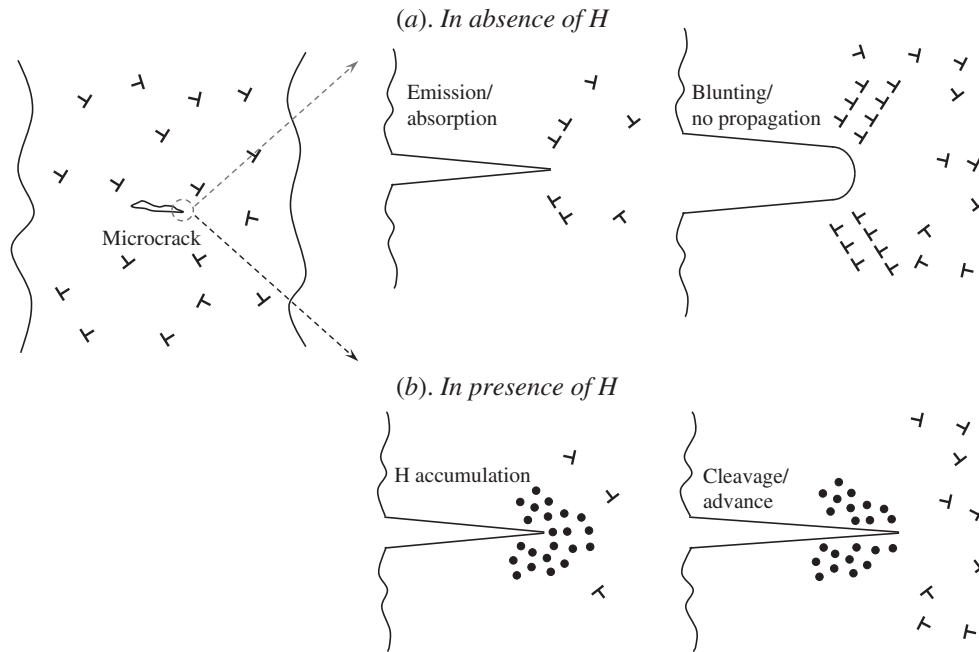


Fig. 1. Schematic showing the evolution of a pre-existing microcrack during loading: (a) in the absence of H, where the crack is blunted by emission and absorption of dislocations, and (b) in the presence of H, where accumulation of H near the crack tip **inhibits emission and absorption**, leading to cleavage fracture.

by a continuum region that can contain discrete dislocations [61–63], and standard large-scale molecular dynamics (MD) simulations.

We consider a variety of crack geometries (I–V) as follows. Using CADD, we first study cracks in single crystal Ni having a $(1\ 1\ 1)$ crack plane normal and $[1\ 1\ 2]$ crack front. This orientation is most favorable for dislocation nucleation and blunting, and thus represents the most challenging geometry for embrittlement. Cracks of different radius of curvature R (bluntness) are created by **removing planes of atoms behind the crack tip**, as shown in Fig. 2a–c. Using MD, we also consider cracks along the grain boundaries in two Ni bi-crystals, as shown Fig. 2d–e, where the crack plane coincides with a $\Sigma 99\ \langle 1\ 1\ 0 \rangle$ and a $\Sigma 9\ \langle 1\ 1\ 0 \rangle$ symmetric tilt grain boundary, respectively. In all geometries, the simulation cell is periodic along the line of the crack front with a period larger than twice the cut-off distance ($5.65\ \text{\AA}$) of the interatomic potential. In the CADD single crystal models, the atomistic domain has dimensions $L_x \times L_y \times L_z$ in the ranges $L_x \in [86.3, 200.0]\ \text{\AA}$, $L_y \in [106.8, 200.0]\ \text{\AA}$ and $L_z = 15.0\ \text{\AA}$ with larger L_x and L_y used when the nanohydride phase becomes large, and a surrounding continuum domain of size $2000\ \text{\AA} \times 2000\ \text{\AA}$. In the MD models for grain boundaries, the atomistic domain has dimensions $480\ \text{\AA} \times 480\ \text{\AA} \times 15\ \text{\AA}$. The crack is loaded by applying displacements on the outer boundary of the overall simulation cell corresponding to the anisotropic elastic mode I stress intensity field K_I [32]. **The phenomena at the crack tip (dislocation emission or crack growth) are examined as a function of the applied loading and the extent of the nanohydride formed around the crack tip (see below).**

We model the Ni–H system using the **embedded-atom-method (EAM) potentials** [64,65] developed by Angelo et al. [66] for Ni and H but with an important modification. The original potential of Angelo et al. predicts a negative shear modulus C_{44} for the cubic NiH hydride, so that the cubic hydride is unstable to shear. Since cubic NiH is the physically correct phase, with a shear modulus of 41 GPa as computed by first-principles methods [67], the published potential cannot be used for materials with possibly high H content. To obtain the correct stable hydride and maintain otherwise reasonable properties of the Ni–H system, we have studied the effects of variations of the cut-off distance r_{cut} used for the pair potential and the electron density functions of Ni. Table 1 shows that small increases in the cut-off radius beyond the value of $r_{\text{cut}} = 4.84\ \text{\AA}$ used in the original formulation [66], can significantly increase C_{44} , generating a stable cubic NiH phase while leading to minor changes (in some cases, improvements) in other properties of both Ni and Ni–H. Here, we use **$r_{\text{cut}} = 4.90\ \text{\AA}$** , which provides a good overall balance of properties for Ni, Ni with dilute H, and the NiH phase.

2.2. Hydride formation around the crack tip

In a Ni lattice, the dissolved H atoms occupy **octahedral interstitial sites** or certain polyhedral interstitial holes along grain boundaries [46]. Using a simple solution model, the equilibrium H concentration $c(x)$ at site x can be determined by the energy difference $\Delta E(x)$ between an H atom at position x and an H atom in the bulk crystal under zero load as [45]

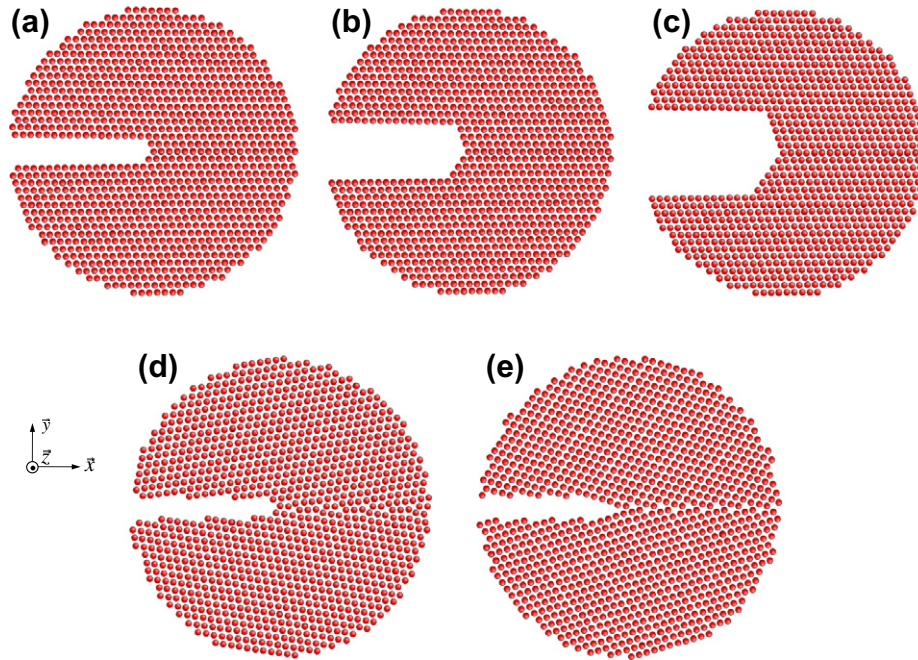


Fig. 2. Atomistic configurations of the crack geometries studied in this work: cracks in single crystals with radii of curvature (a) $R = 0.5$ nm, (b) $R = 0.9$ nm, and (c) $R = 1.3$ nm, and along bi-crystal symmetric tilt grain boundaries of types (d) $\Sigma 99$ $(1\ 1\ 0)$ and (e) $\Sigma 9$ $(1\ 1\ 0)$ with $R = 0.5$ nm. Configurations are projection views along the crack line and show only a small circular region around the crack tip. In all cases, the crystal is oriented with $x = [1\ 1\ 2]$ and $y = [1\ 1\ 1]$, which allows for dislocation emission from the crack tip.

Table 1

Properties of the Ni–H system as the potential cut-off distance r_{cut} for Ni varies: cohesive energy E_{coh} ; lattice constant a_0 ; elastic constants C_{11} , C_{12} and C_{44} ; surface energies γ_{100} , γ_{110} and γ_{111} for $(1\ 0\ 0)$, $(1\ 1\ 0)$ and $(1\ 1\ 1)$ surfaces, respectively; stable and unstable stacking fault energies γ_{sf} and γ_{usf} ; vacancy formation energy E_{v} ; H migration barrier E_{m} ; and H partial volume $\Delta V/V$. The original Angelo et al. potential employs $r_{\text{cut}} = 4.84$ Å.

	$r_{\text{cut}} = 4.84$ Å		$r_{\text{cut}} = 4.86$ Å		$r_{\text{cut}} = 4.88$ Å		$r_{\text{cut}} = 4.90$ Å	
	Ni	NiH	Ni	NiH	Ni	NiH	Ni	NiH
E_{coh} (eV)	−4.45	—	−4.48	—	−4.50	—	−4.53	—
a_0 (Å)	3.520	3.741	3.521	3.738	3.523	3.737	3.524	3.736
C_{11} (GPa)	246.4	238.1	246.9	246.4	249.7	264.2	251.7	281.2
C_{12} (GPa)	147.3	183.0	146.1	186.2	146.8	193.7	147.3	200.9
C_{44} (GPa)	124.8	−0.94	127.3	7.5	129.2	16.3	130.6	24.6
γ_{100} (erg cm $^{-2}$)	2060	—	2082	—	2104	—	2126	—
γ_{110} (erg cm $^{-2}$)	2350	—	2372	—	2392	—	2412	—
γ_{111} (erg cm $^{-2}$)	1928	—	1951	—	1967	—	1994	—
γ_{sf} (erg cm $^{-2}$)	88.8	—	105.5	—	122.4	—	155.2	—
γ_{usf} (erg cm $^{-2}$)	212.3	—	229.5	—	246.3	—	276.5	—
E_{v} (eV)	1.59	—	1.62	—	1.64	—	1.66	—
E_{m} (eV)	0.46	—	0.46	—	0.46	—	0.46	—
$\Delta V/V$	0.31	—	0.31	—	0.31	—	0.31	—

$$c(x) = \frac{c_0 \exp[\Delta E(x)/k_B T]}{1 + c_0 \exp[\Delta E(x)/k_B T]} \quad (1)$$

where c_0 is the equilibrium H concentration (H atoms per Ni) in an unstressed bulk crystal, T is the temperature, and positive $\Delta E(x)$ corresponds to binding, favoring segregation to site x relative to the bulk crystal. In any given system, c_0 is determined by an externally imposed chemical potential μ at temperature T , and so here we use c_0 to reflect the imposed chemical potential, whether generated by electrochemical or gas-phase methods.

In an inhomogeneous material, due to the presence of surfaces, grain boundaries, or stress, the concentration $c(x)$ is equivalent to the probability of finding an H atom at position x . The energy $\Delta E(x)$ is the energy change of the system into which the H is introduced, and must include the energy due to interactions arising from the presence of other H atoms; i.e. the energy $\Delta E(x)$ must be determined fully self-consistently. In the presence of a loaded crack, a major component of the energy is the elastic interaction energy $p(x)\Delta V$ [40,49] where $p(x) = \sum_{i=1}^3 \sigma_{ii}(x)/3$ is the crack-induced pressure field at position x and ΔV is

the misfit volume of the H atom. However, $p(x)\Delta V$ alone is not sufficient because when an H atom is inserted into Ni it locally expands the lattice and increases $\Delta E(x)$ for subsequent H atoms in its vicinity. As a result, $\Delta E(x)$ depends on both the applied loading and the overall instantaneous concentration profile $c(x)$. Achieving a proper thermodynamic equilibrium distribution of H atoms around the loaded crack thus requires some care. One approach is to use grand canonical Monte Carlo in which H atoms are repeatedly added and removed from the system according to a stochastic algorithm that ensures that the chemical potential is constant throughout the system. Here, we use a new approach, described below, that generates the same final equilibrium H distribution but with some potential computational advantages.

We consider a crack subject to an increasing mode I loading and prior to any dislocation emission or cleavage. We have shown [45] that even for very small values of c_0 (appm), the energy of H on Ni surfaces is sufficiently negative so that full surface coverage ($c = 1$) is predicted. We therefore initially cover the crack surfaces with H at $c = 1$. In the first step, we numerically compute the energy $\Delta E_1(x)$ for introduction of a single H at each possible site x in the system, measured relative to H far from the crack tip, and calculate the corresponding $c_1(x)$ for each site from Eq. (1) given c_0 and T . We then insert H atoms into those sites according to a probability $P_1(x) = c_1(x)$. We then calculate the energies $\Delta E_2(x)$ for putting an H atom into each remaining unoccupied site. Since the local expansion due to inserted H atoms favors the insertion of additional H, we find that $\Delta E_2(x)$ is always greater than $\Delta E_1(x)$. Thus, additional H atoms should be introduced into the system while previously inserted H atoms remain. To insert new atoms, however, we must account for the fact that these sites were not occupied in the previous step. After the second insertion, the concentration of H at an interstitial site x should equal $c_2(x)$, the equilibrium concentration computed from Eq. (1) using the energy $\Delta E_2(x)$. Thus, the probability $P_2(x)$ for insertion into site x must satisfy

$$c_1(x) + (1 - c_1(x))P_2(x) = c_2(x), \quad (2)$$

and hence

$$P_2(x) = \frac{c_2(x) - c_1(x)}{1 - c_1(x)} \quad (3)$$

H atoms are thus introduced into unoccupied sites with probability $P_2(x)$. In the n th step, with the energy for insertion of a new H atom into an unoccupied site denoted as $\Delta E_n(x)$ and the corresponding true concentration denoted as $c_n(x)$, the probability of insertion of an H is

$$P_n(x) = \frac{c_n(x) - c_{n-1}(x)}{1 - c_{n-1}(x)} \quad (4)$$

Eq. (4) is easily established using basic statistics. When the concentration reaches the correct equilibrium value, then $c_n(x) = c_{n-1}(x)$ and $P_n(x) = 0$, so that the insertion process converges. We study increasing applied loads, so that the

binding energies for H around the crack tip are steadily increasing. Thus, the fully self-consistent H distribution obtained at one applied load is used as the starting point for subsequent insertions of H at the next load increment.

3. Results

3.1. Nanohydride formation and fracture

Using the stochastic procedure described above, we examine the evolution of equilibrium H atmospheres with increasing mode I loading around the various crack-tip geometries. In all geometries studied, dislocation emission is favored in the hydrogen-free material, with emission occurring at stress intensities K_I^c between 0.69 and 0.77 MPa $\sqrt{\text{m}}$, which are lower than the stress intensities for cleavage K_I^c that lie between 0.95 and 1.04 MPa $\sqrt{\text{m}}$. The K_I^c values are computed using $K_I^c = \sqrt{\frac{\Gamma}{A_1}}$ [68], where Γ is the fracture surface

energy and $A_1 = [\frac{\sqrt{a_{22}}}{2} \sqrt{\frac{a_{22}}{a_{11}} + 2a_{12} + a_{66}}]^{-1}$ depends on the anisotropic plane-strain elastic moduli a_{ij} [69]. We thus start our calculations at $K_I = 0.64$ MPa $\sqrt{\text{m}}$, below K_I^c . We use far-field H concentrations in the range $c_0 = 4 \times 10^{-6}$ – 1.3×10^{-4} corresponding to H_2 gas pressures ranging from 1 to 1000 atm at room temperature, conditions under which a wide spectrum of H embrittlement experiments have been conducted.

Representative examples of the equilibrium distributions of H around the crack tip are shown in Fig. 3 at $c_0 = 4 \times 10^{-6}$, 2×10^{-5} , and 4×10^{-5} , and $T = 300$ K for geometries I, II and IV at $K_I = 0.64$ MPa $\sqrt{\text{m}}$. Substantial H accumulation can occur around the crack tip despite the small c_0 , with the concentration $c(x) \sim 1$ very near the tip, indicating the formation of a “nanohydride” around the crack tip. The nanohydrides form with different sizes and shapes depending on the geometry and symmetry of the system. Comparing Fig. 3a–c and Fig. 3d–f, a smaller radius of curvature leads to a thicker nanohydride, consistent with the higher stresses around a sharper crack. Comparing Fig. 3a–c and Fig. 3g–i, the nanohydride in a single crystal is asymmetric with respect to the crack line, reflecting the crystal anisotropy, while the hydride remains symmetric around a symmetric tilt bi-crystal crack plane. The nanohydride also extends further along the grain boundary due to energetically favorable H sites along the grain boundary as compared to bulk Ni.

In the presence of H around the crack tip, dislocation emission can be inhibited such that the applied load can be increased beyond K_I^c . Increased loading then allows for further accumulation of H atoms near the crack tip, which can further suppress dislocation emission. If sufficient H accumulation can occur with increasing load to continually suppress dislocation emission, then cleavage fracture can occur instead of dislocation emission and blunting. This embrittlement mechanism is explicitly illustrated for two different crack geometries in Figs. 4 and 5

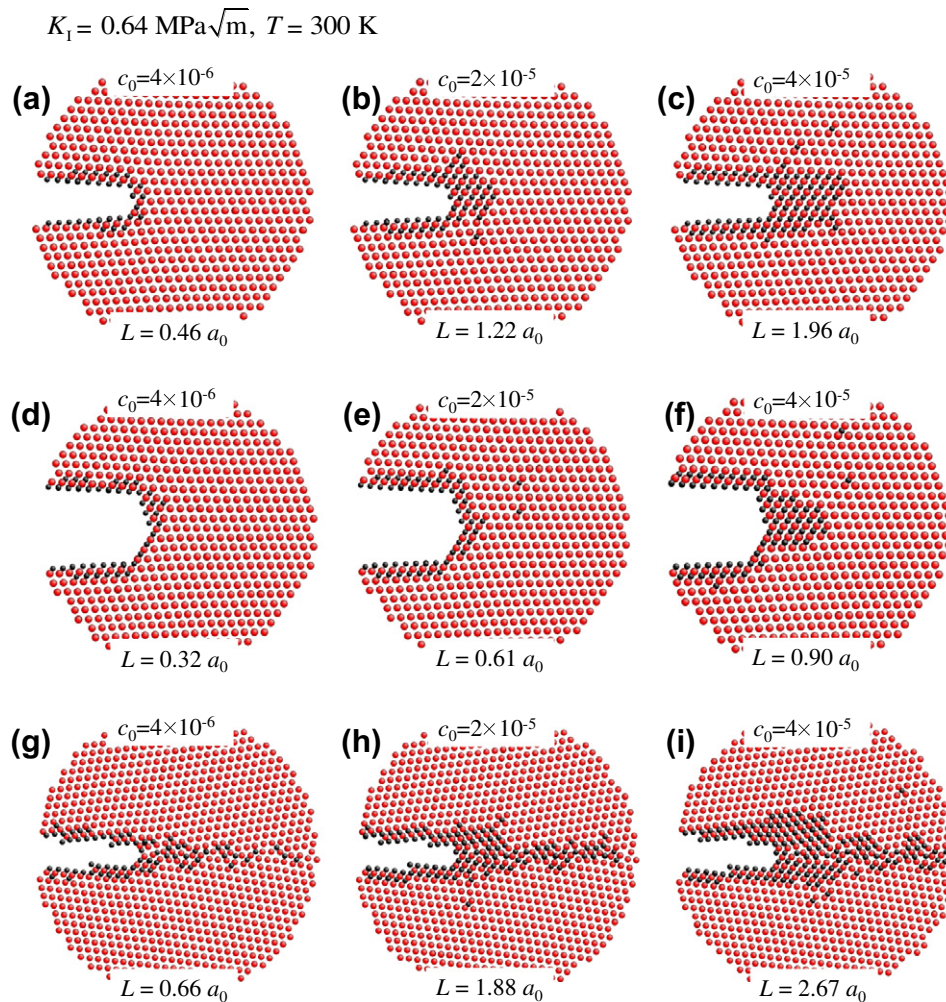


Fig. 3. Atomistic configurations of equilibrium nanohydride phases developed at $T = 300 \text{ K}$ and $K_I = 0.64 \text{ MPa}\sqrt{\text{m}}$ for various bulk H concentrations, i.e. (a)–(c) for geometry I cracks, (d)–(f) for geometry II cracks, and (g)–(i) for geometry IV cracks. Atoms are projected into the plane along the crack line, with Ni atoms in red and H atoms in black. The H concentration along the projected direction is $c \sim 1$ in the nanohydride except at the nanohydride/Ni interface and at occasional isolated H sites away from the nanohydride (For interpretation of the references to color in this figure legend, the reader is referred to the web version of this article.).

for $c_0 = 4 \times 10^{-6}$, $T = 300 \text{ K}$ corresponding to an H_2 gas pressure of 1 atm. Figs. 4 and 5 show the sequence of equilibrium H configurations around the crack tip with increasing K_I . With increasing load, the crack tip becomes completely surrounded by a growing nanohydride, which prevents dislocation emission and finally culminates in brittle cleavage through most of the nanohydride phase (Figs. 4e and 5e). The demonstration of a brittle-to-ductile transition at the nanoscale crack tip clearly confirms the scenario of H embrittlement proposed above.

The K_I values at cleavage in Figs. 4 and 5 are 2.06 and 1.95 $\text{MPa}\sqrt{\text{m}}$, respectively. These are much higher than the predicted Griffith K_I^c for the Ni–H phase because the nanohydride phase has a volume expansion of 19.2% relative to the Ni matrix which generates a high hydrostatic compression in the constrained hydride [50,70], decreasing the effective stress intensity at the local crack tip and thus requiring a much higher applied K_I to induce cleavage. In spite of the increased applied stress intensity, there is no

crack-tip blunting and thus no ability to make a transition to ductile failure.

An important aspect of the embrittlement mechanism here is the maintenance of a sharp crack tip after cleavage. We further postulate that after cleavage the H atoms behind the new crack tip experience a high driving force for nanometer-scale diffusion to positions ahead of the new crack, re-establishing the nanohydride, and allowing the cleavage process to be repeated. Macroscopic crack growth thus results from continued nanocleavage and reprecipitation of the nanohydride. We have observed this in explicit molecular dynamics modeling of the rearrangement/transport of H atoms after cleavage, but such kinetic modeling requires tricks and constraints, and so is beyond the scope of this paper and will be addressed in a forthcoming study.

To gain a broader picture of the conditions required to obtain embrittlement, we proceed as follows. For an equilibrium H atmosphere generated at a given c_0 , T , and applied K_I , we increase the applied loading while holding

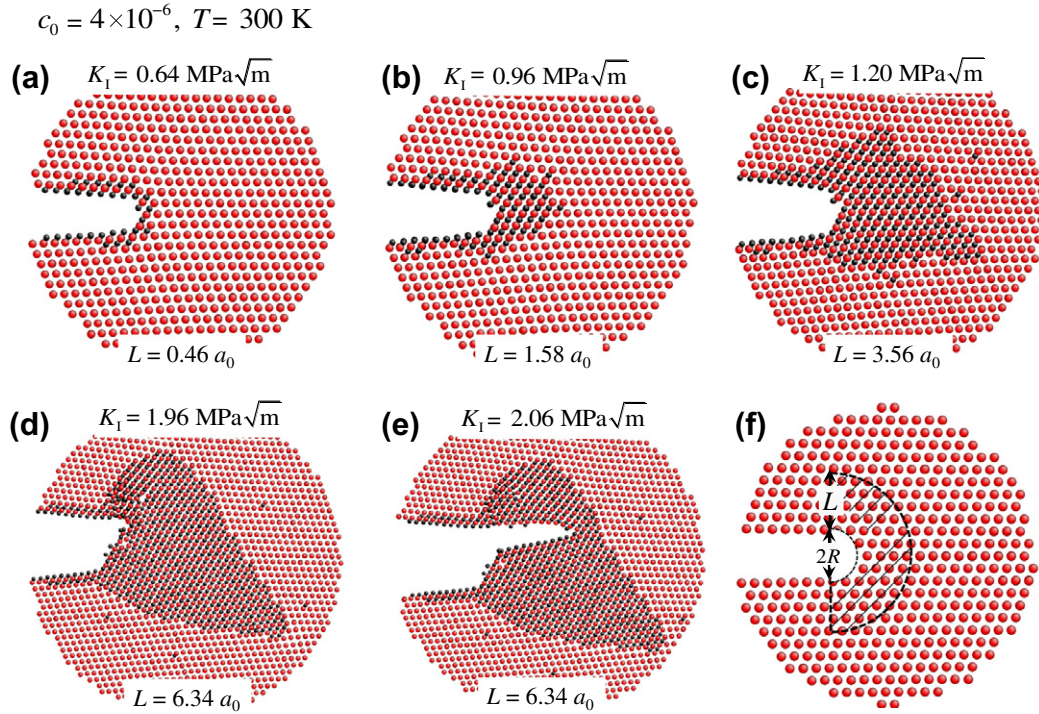


Fig. 4. Example of evolution of the nanohydride phase around a geometry I crack tip at $c_0 = 4 \times 10^{-6}$ and $T = 300$ K with increasing load (a)–(d) and (e) configuration at $1.96 \text{ MPa}\sqrt{\text{m}}$ after loading to $K_I = 2.06 \text{ MPa}\sqrt{\text{m}}$, where cleavage through the nanohydride occurs. (f) Schematic of simple geometry for characterizing the size L of nanohydrides. Ni atoms are red and H atoms are black. All figures show projection views along the crack line. The H concentration along the projected direction is $c \sim 1$ in the nanohydride except at the nanohydride/Ni interface and at occasional isolated H sites away from the nanohydride (For interpretation of the references to color in this figure legend, the reader is referred to the web version of this article.).

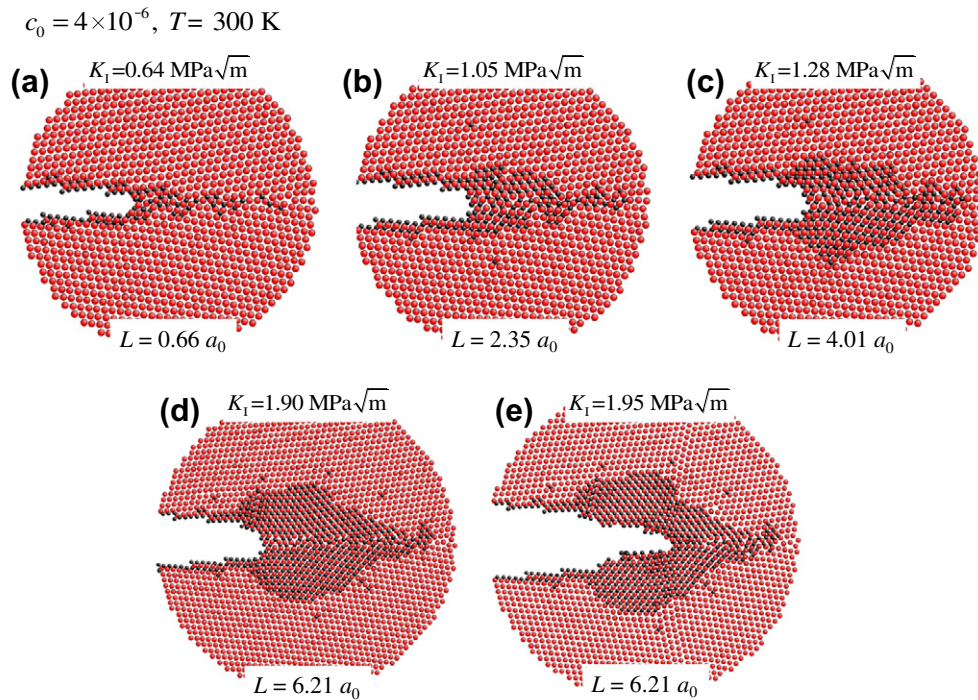


Fig. 5. Example of evolution of the nanohydride phase around a geometry IV crack tip at $c_0 = 4 \times 10^{-6}$ and $T = 300$ K with increasing load (a)–(d) and (e) configuration at $1.90 \text{ MPa}\sqrt{\text{m}}$ after loading to $K_I = 1.95 \text{ MPa}\sqrt{\text{m}}$, where cleavage through the nanohydride occurs. Ni atoms are red and H atoms are black. All figures show projection views along the crack line. The H concentration along the projected direction is $c \sim 1$ in the nanohydride except at the nanohydride/Ni interface and at occasional isolated H sites away from the nanohydride (For interpretation of the references to color in this figure legend, the reader is referred to the web version of this article.).

the H atmosphere fixed (corresponding to rapid loading relative to the rate of H transport to the crack tip) and examine the crack-tip deformation behavior. When the nanohydride is very small or poorly formed, dislocation emission can still occur prior to cleavage. For instance, for the atomistic configurations shown in Fig. 3a–c developed at $K_I = 0.64$ MPa $\sqrt{\text{m}}$, we observe dislocation emission at $K_I = 0.83$, 1.07 and 1.39 MPa $\sqrt{\text{m}}$, respectively. These values are all above the K_I^e for pure Ni but emission still does occur, initiating crack blunting. For all the geometries and far-field concentrations studied here, we have collected data on dislocation emission or cleavage as a function of the load level at which the H atmosphere was formed. The behavior can be well-characterized in terms of the size of the nanohydride. For simplicity, we characterize the nanohydride geometry has a half-annulus of inner radius R , corresponding to the crack-tip radius of curvature, annular thickness L , and length L_z parallel to the crack line, as illustrated in Fig. 4f. If a total number N_H of H atoms are accumulated around the crack tip, then the effective thickness of the nanohydride phase is

$$L = \sqrt{\frac{N_H a_0^3}{2\pi L_z} + R^2} - R \quad (5)$$

Geometries I, IV, and V have $R \sim 0.5$ nm, while geometries II and III have $R = 0.9$ nm and 1.3 nm, respectively. For a given nanohydride, now characterized by L , the load level K_I at which some event occurs (emission or cleavage) is shown in Fig. 6. In all cases, the K_I required for any event increases with increasing L and, moreover, the event changes from dislocation emission to brittle cleavage when $L > 3a_0$. Once the cleavage regime is reached, K_I continues to increase with increasing L due to the hydrostatic compression in the nanohydride but eventually saturates so that cleavage is independent of the nanohydride size. The transition from emission events to cleavage events does not depend significantly on the crack-tip geometry – either the radius or the presence of a grain boundary.

The saturation cleavage value of K_I for larger nanohydrides does depend on the boundary undergoing fracture, with grain boundaries showing cleavage at lower values of K_I than in the single crystal. This behavior is not surprising, since the grain boundary fracture energies (both with and without H) are lower than in the single crystal. Thus, grain boundaries do provide a low-energy cleavage path, so that intergranular fracture is favored over transgranular fracture, as observed experimentally. In addition, pre-existing microcracks are likely to reside along grain boundaries. However, the basic transition from ductile (dislocation emission) to brittle (cleavage in the nanohydride) does not depend strongly on the existence of grain boundaries.

Fig. 6b shows that K_I vs. L is nearly independent of the crack-tip blunting R in a single crystal. This is a bit counter-intuitive but the actual geometries I–III in Fig. 2 have very similar local atomic arrangements at the crack tip.

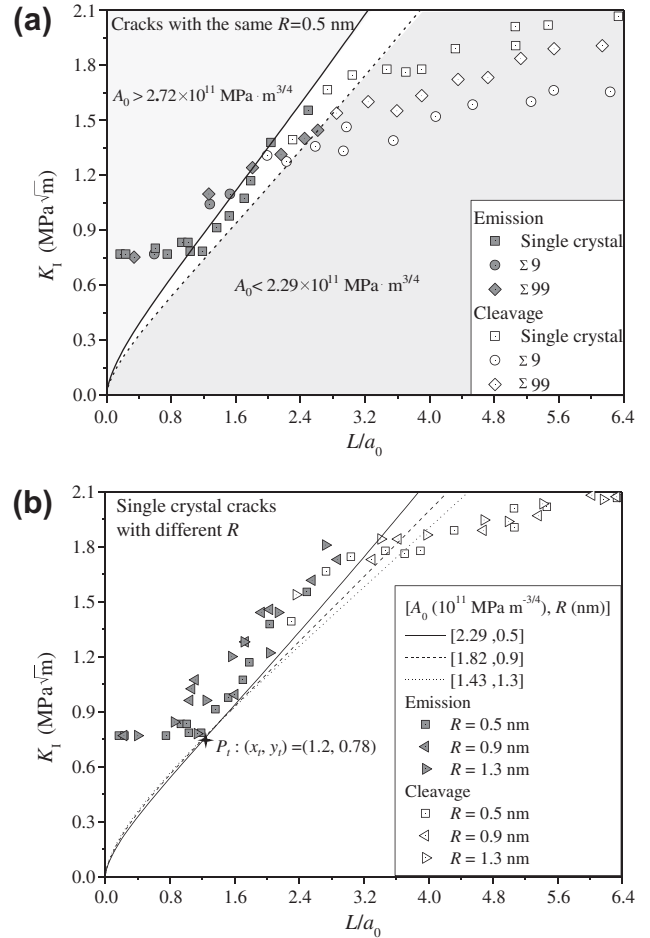


Fig. 6. Simulated stress intensity K_I at which either dislocation emission or brittle cleavage occurs as a function of nanohydride of thickness L for all crack geometries and H concentrations studied. Filled symbols: dislocation emission. Open symbols: cleavage fracture. (a) Crack geometries with $R = 0.5$ nm and (b) single crystal cracks with varying radii R . Also shown in (a) are K_I vs. L curves calculated from the kinetic model (Eq. (16)) for two values A_0 , showing that brittle cleavage is predicted for $A_0 < 2.29 \times 10^{11} \text{ MPa m}^{-3/4}$ (shaded region on the right of the dashed curve) and ductile dislocation emission is predicted for $A_0 > 2.72 \times 10^{11} \text{ MPa m}^{-3/4}$ (i.e. the shaded region on the left of the solid curve). Also shown in (b) are K_I vs. L curves calculated from the kinetic model (Eq. (16)) for critical values of A_0 for each crack radius.

Since both dislocation emission and cleavage initiate at the local crack tip where the stress field is determined by the local geometry, the independence of K_I is less surprising.

3.2. Kinetics of formation of a crack-tip nanohydride

Our simulations above show that a nanohydride phase can form around a crack tip and drive a transition to brittle cleavage. Whether this phenomenon can occur in any given system depends on the hydrogen environment, temperature, loading rate, loading geometry, and initial microcracks, among other variables. Expecting that the bulk concentration c_0 of H in a material is small, the formation and growth of the nanohydride depends on the rate of H

diffusion to the vicinity of a crack tip. Here, we provide a basic analysis of the H diffusion process, culminating in a mechanism map for embrittlement as a function of material and loading conditions.

We consider a pre-existing microcrack that is subjected to an external load that generates a near-tip mode I loading rate \dot{K}_I . At time t , the stress intensity is then $K_I = \dot{K}_I t$ and the stress field is, assuming isotropic elasticity,

$$\begin{aligned}\sigma_{xx} &= \frac{\dot{K}_I t}{\sqrt{2\pi r}} \cos \frac{\theta}{2} \left(1 - \sin \frac{\theta}{2} \sin \frac{3}{2} \theta \right), \\ \sigma_{yy} &= \frac{\dot{K}_I t}{\sqrt{2\pi r}} \cos \frac{\theta}{2} \left(1 + \sin \frac{\theta}{2} \sin \frac{3}{2} \theta \right), \\ \sigma_{zz} &= \nu(\sigma_x + \sigma_y),\end{aligned}\quad (6)$$

where (r, θ) are polar coordinates with $\theta \in (-\pi, \pi]$ measured from the crack tip and ν denotes the Poisson ratio. The hydrostatic stress p is then

$$p = \frac{1}{3}(\sigma_{xx} + \sigma_{yy} + \sigma_{zz}) = \frac{2(1+\nu)}{3\sqrt{2\pi r}} \dot{K}_I t \cos \frac{\theta}{2} \quad (7)$$

The chemical potential for an H atom at r can be written, using simple solution theory, as

$$\mu = \mu_0 + k_B T \ln \frac{c}{1-c} + p\Omega \quad (8)$$

where c is the equilibrium H concentration at (r, θ) , Ω is the partial volume of H, k_B is the Boltzmann constant, and μ_0 is a constant. The driving force for H atom diffusion toward the crack tip is then

$$\vec{F} = -\nabla\mu = -k_B T \frac{1}{c(1-c)} \nabla c + \Omega \nabla p \quad (9)$$

Away from the immediate crack tip, the H concentration $c \ll 1$ is small and so the dominant driving force is due to the pressure field of the crack so that

$$\vec{F} = \frac{(1+\nu)\Omega\dot{K}_I t}{3\sqrt{2\pi}} \frac{\cos(\theta/2)}{r^{3/2}} \vec{e}_r - \frac{(1+\nu)\Omega\dot{K}_I t}{3\sqrt{2\pi}} \frac{\sin(\theta/2)}{r^{3/2}} \vec{e}_\theta \quad (10)$$

with \vec{e}_r being a unit radial vector pointing towards the crack tip and \vec{e}_θ being a unit angular vector. The radial velocity of H atoms toward the crack tip is then

$$v_r = -\frac{dr}{dt} = \frac{D\Omega}{k_B T} \frac{(1+\nu)\dot{K}_I t}{3\sqrt{2\pi}} \frac{\cos(\theta/2)}{r^{3/2}} \quad (11)$$

where D is the effective diffusion coefficient of H in bulk Ni at T . The effective H diffusion coefficient can be influenced by trapping at voids, dislocations, or other defects in the bulk of the material, and so does not necessarily correspond to simple diffusion of H through the interstitial lattice in an ideal Ni single crystal. The time t required for a hydrogen atom initially at r to arrive at the crack tip $r \sim 0$ is then obtained by integrating Eq. (11), leading to

$$r = \left(\frac{5(1+\nu)D\Omega\dot{K}_I t^2 \cos(\theta/2)}{12\sqrt{2\pi}k_B T} \right)^{\frac{2}{3}} \quad (12)$$

The precise final position $r \sim 0$ is not important – the time is controlled by the flow of H from far away into the crack region. Note that away from the crack tip, the H concentration is always quite low and so it is sufficient to use the effective diffusion coefficient for dilute H throughout the material and neglect any explicit concentration dependence of diffusion. The aggregation and redistribution of H locally at the crack tip are fast processes relative to the time required for H to reach the near-crack-tip region. Thus the H kinetics in and around the nanohydride does not influence the analysis here. We have examined the concentration-dependent H diffusion in another study [71] where H concentration effects are important, but can conclude that our use of the dilute limit here is valid for the current problem.

From Eq. (12), the number N_H of H atoms that have diffused to the vicinity of the crack tip at time t is then

$$N_H = \frac{1}{2} L_z c_0 \int_{-\pi}^{\pi} r^2 d\theta \simeq 2.1 L_z c_0 \left(\frac{5(1+\nu)D\Omega\dot{K}_I t^2}{12\sqrt{2\pi}k_B T} \right)^{\frac{4}{3}} \quad (13)$$

via Eq. (5), the size L of the nanohydride formed at time t satisfies

$$\frac{\pi}{2}(L+R)^2 - \frac{\pi}{2}R^2 = 2.1 c_0 \left(\frac{5(1+\nu)D\Omega\dot{K}_I t^2}{12\sqrt{2\pi}k_B T} \right)^{\frac{4}{3}} \quad (14)$$

Using $K_I = \dot{K}_I t$, we obtain the nanohydride size L as a function of K_I given by

$$L = \sqrt{R^2 + \left(\frac{K_I}{A_0} \right)^{\frac{8}{3}}} - R \quad (15)$$

where

$$A_0 = \left(\frac{1.67\sqrt{2\pi}k_B T}{(1+\nu)D\Omega} \right)^{1/2} c_0^{-\frac{5}{3}} \dot{K}_I^{\frac{1}{3}} \quad (16)$$

is the single parameter that combines the effects of concentration, diffusion coefficient, stress intensity loading rate, and temperature that controls the kinetics of formation of the nanohydride.

3.3. Mechanism map for H embrittlement

We now combine our simulation measurements of embrittlement as a function of nanohydride size with the kinetics of nanohydride formation contained in Eq. (15). Specifically, we invert Eq. (15) to obtain K_I vs. L for various values of A_0 and R and compare the results to the simulations, as shown in Fig. 6. Two distinct domains of behavior are found. For small A_0 , conditions are such that the nanohydride can form sufficiently well to prevent dislocation nucleation and lead to cleavage embrittlement. Small A_0 (embrittlement) corresponds to higher bulk H concentration, slower loading rate, and/or faster diffusion of H, although each factor enters with a different scaling. For large A_0 , the nanohydride is insufficient to inhibit emission, so that the material response remains ductile due to crack-tip

blunting. Large A_0 (no embrittlement) corresponds to lower bulk H concentration, faster loading rate, and/or slower H diffusion. The transition from ductile-to-brittle occurs in a fairly narrow range of A_0 . For a sharp crack ($R = 0.5$ nm), there is an approximate critical value of $A_0 \sim 2.29 \times 10^{11} \text{ MPa m}^{-3/4}$ that delineates the brittle and ductile regimes. As R increases (Fig. 6b), the critical A_0 for the ductile-to-brittle transition decreases only slightly (i.e. $A_0 = 2.29, 1.82$ and $1.43 \times 10^{11} \text{ MPa m}^{-3/4}$ for $R = 0.5, 0.9$ and 1.3 nm respectively).

To condense the mechanism map in Fig. 6 even further, we note that for all cases, the K_I vs. L at the critical A_0 value intersects the simulated K_I^c vs. L data at nearly a single point $L/a_0 = 1.2$, $K_I = 0.78 \text{ MPa } \sqrt{\text{m}}$ (see Fig. 6). At this point, we obtain a single inequality for embrittlement that relates all of the material and testing parameters

$$\frac{R}{a_0} + 0.6 < 0.09 c_0 D^{\frac{4}{5}} \left(\frac{k_B T}{(1+\nu)\Omega} \right)^{\frac{4}{5}} \dot{K}_I^{\frac{4}{5}} a_0^{-2} (\text{MPa } \sqrt{\text{m}})^{\frac{8}{5}}. \quad (17)$$

Eq. (17) relates R , c_0 , D , K_I , and T at the critical point for the transition to embrittlement. Any combination of parameters for which the right-hand side of Eq. (17) exceeds the left-hand side will lead to embrittlement. We will apply Eq. (17) below in making a comparison to experiments on embrittlement in the Ni–H system, recognizing that it captures the more general behavior shown in Fig. 6.

3.4. Preliminary comparison to experiments

Bechtel et al. [2] recently measured ductility and the propensity for intergranular fracture in experiments on several polycrystalline Ni specimens pre-charged with H. Unnotched tensile specimens were loaded at a constant strain rate $\dot{\epsilon} = 0.0004 \text{ s}^{-1}$ at $T = 300 \text{ K}$ until fracture. Bechtel et al. found strong embrittlement in specimens charged with $c_0 \sim 10^{-3}$ and above. They also found embrittlement is delayed until higher c_0 for specimens having a high fraction of special grain boundaries. Here, we make some contact with those experiments.

We use the lattice constant of Ni $a_0 = 3.52 \text{ Å}$, the partial volume of H in Ni $\Omega = 3.39 \text{ Å}^3$, and the Young's modulus is $E = 250 \text{ GPa}$ with Poisson ratio $\nu = 0.31$ [66]. To apply the model, we postulate the existence of initial microcracks having length equal to the grain size in the material, grain size $d \sim 30 \text{ } \mu\text{m}$, a common assumption in modeling the strength of ceramics. Then, the loading rate \dot{K}_I is related to the strain rate $\dot{\epsilon}$ and the averaged grain size d as

$$\dot{K}_I = E \dot{\epsilon} \sqrt{2\pi d} \simeq 1.77 \text{ MPa } \sqrt{\text{m}} \text{ s}^{-1} \quad (18)$$

At $T = 300 \text{ K}$, Eq. (17) predicts a domain of embrittlement in terms of c_0 , R and D . Fig. 7 shows the iso-concentration lines required for embrittlement as a function of the H diffusion rate D and microcrack radius R . For a particular c_0 , embrittlement is expected in the region to the right side of the line.

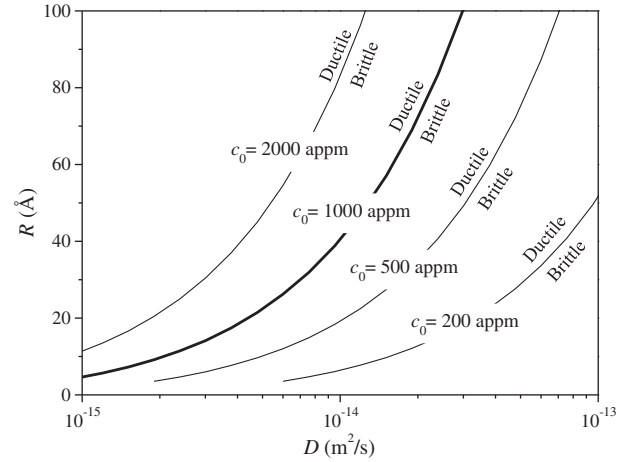


Fig. 7. Relation between microcrack radius R and H diffusion coefficient D required for the onset of brittle failure at various values of c_0 , as computed using Eq. (17) for Ni–H at the experimental conditions used by Bechtel et al. [2]. Brittle failure at a particular c_0 is expected for any combination of R and D on the right side of the corresponding curve. $c_0 = 1000$ appm corresponds to the concentration at which embrittlement is observed in the Bechtel et al. experiments, which can be achieved for a range of H diffusion and crack-tip radii that are physically reasonable.

The lattice diffusivity of H in a single crystal bulk Ni under zero stress is $D_L = 1.9 \times 10^{-14} \text{ m}^2 \text{ s}^{-1}$ at 300 K [7,66,72]. However, trapping of H at various internal defects (e.g. dislocations, grain boundaries, vacancies, etc.) can greatly affect H migration and lead to an effective diffusivity [56,73–76]:

$$D = D_L \left(1 + K_T \frac{N_T}{N_L} \right)^{-1} \quad (19)$$

where N_T is the number of traps per unit volume, N_L the number of interstitial sites per unit volume in the Ni lattice, and $K_T = \exp[-\Delta E_T/k_B T]$ is the equilibrium constant for the reversible trapping/detrapping reaction having trap binding energy ΔE_T . Estimates of ΔE_T for various trapping sites (i.e. edge and screw dislocation, Lomer–Cottrell lock, tilt grain boundaries, etc.) are 0.1 – 0.33 eV [66] while in plastically deformed materials $N_T/N_L \sim 10^{-4}$ is estimated [73,75]. The effective diffusivity of H could thus range from 1.9×10^{-14} to $5.3 \times 10^{-16} \text{ m}^2 \text{ s}^{-1}$, which is the range shown in Fig. 7. For this range, embrittlement at $c_0 \sim 10^{-3}$ is then predicted for microcrack-tip radii in the range $R = 0.2$ – 6.8 nm , ranging from atomistically sharp to blunt at the nanoscale but still sharp relative to the overall microcrack size. Thus, the experimental results of Bechtel et al. can generally be rationalized by our model using a physically reasonable range of material parameters and no fitting parameters. This comparison is limited, but serves primarily to show that the model proposed here is capable of quantitatively reasonable predictions of embrittlement.

4. Discussion

Here, we discuss our proposed model for H embrittlement within the context of various experimental observations and other theoretical concepts.

First, our conceptual model is quite general. Accumulation of H near a crack tip is expected in materials where interstitial H has an excess volume [77–80]. The development of a “nanohydride” is not essential – what is essential is that sufficient H accumulates to create a material that resists dislocation nucleation at the crack tip. This can be achieved if H can increase the unstable stacking fault energy γ_{usf}^e of the crack-tip material to sufficiently high values since $K_I^e \propto \sqrt{\gamma_{usf}^e}$ [81]. We have previously demonstrated this for Ni–H [45] but it can easily be investigated via first-principles calculations for many systems [82–84]. In Ni–H, the indirect interaction of H atoms helps drive formation of the nanohydride, and thus allows embrittlement to happen more easily than might occur in other materials. However, this is an issue of magnitude rather than phenomenon.

Focusing on Ni–H, hydrides are not frequently observed in Ni although some hydride formation near grain boundaries and specimen surfaces has been reported. We expect that direct experimental observation of the nanohydride formed here to be difficult because the nanohydride leaves little H behind, and any nanohydride at a crack tip would quickly be desorbed when the specimen is removed from the H atmosphere. Careful in situ experiments might permit observation of the nanohydride at a crack tip, however.

The existence of very high concentrations of H near a crack tip has been measured experimentally by Scully et al. [55,76] While not quite at the nanoscale modeled here, the results of Scully et al. point toward H accumulation at very small scales, consistent with our model. In addition, Scully et al. [1] have shown that crack growth rates correlate with H diffusion rates, which is also consistent with our general concept. Modeling of H accumulation using strain-gradient plasticity, which permits crack-tip stresses to greatly exceed the nominal material yield stress, also shows that high local H accumulation is possible. High crack-tip stresses are also developed in discrete dislocation models of fracture, with fracture observed in materials with cohesive stresses an order of magnitude larger than the nominal tensile yield stress. Similarly, our model here at the nanoscale recognizes that the material around the crack tip is elastic – the concept of a plastic yield stress pertains at larger scales – and so the high stresses near the crack tip that drive the H accumulation are fully expected.

The present model does not preclude parallel operation of the HELP mechanism. The HELP mechanism could act on a large region around the crack and influence the flow behavior while the present model accounts for the local embrittlement and transition to intergranular fracture. In our model, the accumulation of H at the crack tip not only inhibits dislocation emission from the crack tip but also can trap incoming dislocations generated by bulk plasticity. This might give rise to accumulated dislocations just outside the H-rich region. Such local dislocation “activity”, if observed via microscopy, might be interpreted as enhanced localized plasticity. Additionally dislocation nucleation could occur

from the nanohydride/matrix interface (see below), which might also contribute to “enhancing” localized plasticity.

Our model is in some ways an extension of the HEDE model. However, an important difference is that here the embrittlement process is not simply because of a reduction in cleavage fracture energy due to equilibrium H along grain boundaries ahead of a crack tip. Rather, our model posits that embrittlement occurs if dislocation emission from the crack tip can be suppressed, which can occur due to H accumulation around the crack tip even if the cleavage fracture energy is not reduced significantly by the presence of H. Of course, if the cleavage energy is reduced sufficiently such that the stress intensity for cleavage is reduced below that for dislocation emission, then embrittlement can occur without the need for H accumulation at the crack tip. Available calculations of H in Ni and in Al suggest, however, that reductions in the cleavage fracture energies due to H are insufficient to drive cleavage fracture.

The present study has been carried out using quasi-static dynamics, effectively zero temperature, with equilibrium H accumulation corresponding to finite temperatures. The nanohydride, which develops very large constraint stresses and very large coherency stresses at the nanohydride/matrix interface, may show other phenomena at finite temperatures. In particular, two phenomena seem possible. First, dislocation nucleation might occur more readily from the nanohydride/matrix interface to relieve the coherency stresses. This would relieve the compressive stresses in the nanohydride phase and possibly make cleavage easier. However, these dislocations do not contribute to crack-tip blunting, and thus do not affect the major mechanism discussed here. In addition, considering the small size of the nanohydride, the dislocation activities stemming from the coherency stress are expected to be very limited, and our observations in MD, where dislocation emission will occur if the appropriate conditions are achieved, show that dislocation emission from the interface is rare. Therefore although the dislocation nucleation from the nanohydride/matrix interface may quantitatively influence our model predictions, it has little effect on the qualitative picture of ductile-to-brittle transition. Second, vacancy nucleation could be enhanced in the vicinity of the nanohydride. Experiments ascribe measured super-abundant vacancy concentrations to exothermic H–V interactions [85,86]. Thus, high vacancy generation in and around the nanohydride could occur, which might weaken the hydride material further or somehow drive vacancy-assisted crack growth. It is not possible, however, at the present time to model the behavior of H at finite temperatures in the presence of a crack because the interatomic potentials for H do not describe gas phase H and H₂. Preliminary simulations show that H evaporates off the crack surfaces and forms unphysical H_n clusters and depletion of the H in the matrix in unphysical ways. Thus, simulations at finite temperature require modified methods and constraints to prevent such behavior. We will report on our progress in this direction

in future work. In addition, we have computed the vacancy formation energy E_v in the Ni–H hydride and find that it is reduced from 1.59 eV in bulk Ni to 1.07 eV in Ni–H, but the resulting vacancy concentration in the Ni–H near the crack tip (i.e. $c_v \sim \exp(-E_v/k_B T)$) would remain very small and not significantly influence the mechanical properties of the nanohydride.

In summary, we have proposed a new mechanism of H embrittlement in metals, and used the Ni–H system to demonstrate the mechanism. Accumulation of H near the crack tip is found to suppress dislocation emission and encourage cleavage, thus driving a transition in fracture behavior from ductile-to-brittle failure. The accumulation of H forms, in essence, a “dislocation-free” zone around the crack tip, which is a theoretical concept proposed in fracture mechanics to explain crack growth in plastically deformed materials [87]. Once the crack cleaves through the region of high H content, the H left behind the new crack tip can diffuse to the tip and continue the process with limited additional accumulation of H. This nanohydride-induced ductile-to-brittle transition has been combined with a kinetic analysis of H transport to the crack-tip region, and a mechanism map for embrittlement has been proposed that relates embrittlement to the competing factors of H concentration, temperature, diffusion rate, and loading rate. Applying the mechanism to recent experiments on Ni–H yields rough agreement using reasonable material parameters. This new embrittlement concept fits within those of various existing mechanisms, but with new features and a framework that makes specific predictions as a function of material properties. The insights here may serve to spur new and more focused studies of the embrittlement process in various metals.

Acknowledgements

The authors acknowledge support of this work by the Office of Naval Research (Grant # N00014-05-1-0504). The authors thank Dr. Srinath Chakravarthy for useful discussions.

References

- [1] Thomas RLS, Scully JR, Gangloff RP. Metall Mater Trans A 2003;34:327.
- [2] Bechtel S, Kumar M, Somerday BP, Launey ME, Ritchie RO. Acta Mater 2009;57:4148.
- [3] Lassila DH, Birnbaum HK. Acta Metall Mater 1986;34:1237.
- [4] Lassila DH, Birnbaum HK. JOM – J Miner Metal Mater Soc 1984;36:62.
- [5] Lee Y, Gangloff RP. Metall Mater Trans A 2007;38A:2174.
- [6] Gangloff RP. Hydrogen assisted cracking of high strength alloys. In: Milne I, Ritchie RO, Karihaloo BL, editors. Comprehensive structural integrity, vol. 6. New York: Elsevier Science; 2003. p. 31.
- [7] Kimura A, Birnbaum HK. Acta Metall Mater 1988;36:757.
- [8] Troiano AR. Trans ASM 1960;52:54.
- [9] Gerberich WW, Marsh P, Hoehn J, Venkateraman S, Huang H. In: Magnin T, Gras JM, editors. Proceedings of the international conference on corrosion–deformation interactions; 1993. p. 633.
- [10] Oriani RA, Josephic PH. Acta Metall Mater 1974;22:1065.
- [11] Gerberich WW, Foeche TJ. In: Moody NR, editor. Hydrogen enhanced decohesion in Fe–Si single crystals: implications to modelling of thresholds. TMS; 1990. p. 687.
- [12] Oriani RA. Berich Bunsengesell Phys Chem 1972;76:848.
- [13] Gerberich WW, Marsh PG, Hoehn JW. Hydrogen induced cracking mechanisms – are there critical experiments? In: Moody NR, Hoehn JW, editors. Hydrogen effects in materials. Warrendale (PA): TMS; 1996.
- [14] Birnbaum HK, Sofronis P. Mater Sci Eng A – Struct 1994;176:191.
- [15] Beacham CD. Metall Mater Trans B 1972;3:437.
- [16] Robertson IM. Eng Fract Mech 2001;68:671.
- [17] Westlake DG. Trans ASM 1969;62:1000.
- [18] Gahr S, Grossbeck ML, Birnbaum HK. Acta Metall Mater 1977;25:125.
- [19] Shih DS, Robertson IM, Birnbaum HK. Acta Metall Mater 1988;36:111.
- [20] Huang H, Gerberich WW. Acta Metall Mater 1994;42:639.
- [21] Marsh PG, Gerberich WW. Acta Metall Mater 1994;42:613.
- [22] Gerberich WW, Oriani RA, Lii MJ, Chen X, Foecke T. Philos Mag A 1991;63:363.
- [23] Cottrell AH, Bilby BA. Proc Phys Soc A 1949:62.
- [24] Ferreira PJ, Robertson IM, Birnbaum HK. Acta Mater 1998;46:1749.
- [25] Ferreira PJ, Robertson IM, Birnbaum HK. Acta Mater 1999;47:2991.
- [26] Sofronis P, Robertson IM. Philos Mag A 2002;82:3405.
- [27] Murakami Y. Int J Fract 2006;138:167.
- [28] Abraham DP, Altstetter CJ. Metall Mater Trans A 1995;26:2859.
- [29] Teter DF, Robertson IM, Birnbaum HK. Acta Mater 2001;49:4313.
- [30] Matsui H, Kimura H, Kimura A. Mater Sci Eng 1979;40:227.
- [31] Matsui H, Kimura H, Moriya S. Mater Sci Eng 1979;40:207.
- [32] Kimura A, Birnbaum HK. Scripta Metall Mater 1987;21:53.
- [33] Boniszewski T, Smith GC. Acta Metall Mater 1963;11:165.
- [34] Abraham DP, Altstetter CJ. Metall Mater Trans A 1995;26:2849.
- [35] Asano S, Otsuka R. Scripta Metall Mater 1978;12:287.
- [36] Asano S, Otsuka R. Scripta Metall Mater 1976;10:1015.
- [37] Watson JW, Shen YZ, Meshii M. Metall Trans A 1988;19:2299.
- [38] Burke J, Jickels A, Maulik P, Mehta L. Effect of hydrogen on the behavior of materials. Warrendale: TMS; 1976.
- [39] Hardie D, McIntyre P. Metall Trans 1973;4:1247.
- [40] Flanagan TB, Mason NB, Birnbaum HK. Scripta Metall Mater 1981;15:109.
- [41] Takano S, Suzuki T. Acta Metall Mater 1974;22:265.
- [42] Birnbaum HK. MRS Bull 2003;28:479.
- [43] Rice JR. Hydrogen and interfacial cohesion. In: Thompson AW, Bernstein IM, editors. Effect of hydrogen on behavior of materials. Metallurgical Society of AIME; 1976. p. 455.
- [44] Rice JR, Thomson R. Philos Mag 1974;29:73.
- [45] Song J, Soare M, Curtin WA. Model Simul Mater Sci 2010:18.
- [46] Huang S, McDowell DL, Zhu T. Hydrogen embrittlement of metals; personal communication.
- [47] Jiang DE, Carter EA. Acta Mater 2004;52:4801.
- [48] Novak P, Yuan R, Somerday BP, Sofronis P, Ritchie RO. J Mech Phys Solids 2010;58:206.
- [49] Lufrano J, Sofronis P, Birnbaum HK. J Mech Phys Solids 1996;44:179.
- [50] Lufrano J, Sofronis P, Birnbaum HK. J Mech Phys Solids 1998;46:1497.
- [51] Takai K, Shoda H, Suzuki H, Nagumo M. Acta Mater 2008;56:5158.
- [52] Lu G, Kaxiras E. Phys Rev Lett 2005:94.
- [53] Moody NR, Robinson SL, Perra MW. Eng Fract Mech 1991;39:941.
- [54] Moody NR, Robinson SL. In: Magnin T, Gras JM, editors. International conference on corrosion–deformation interactions. Paris; 1993. p. 389.
- [55] Young GA, Scully JR. In: Moody NR, Thompson AW, Ricker RE, Was GW, Jones RH, editors. Hydrogen production, adsorption and transport during environment assisted cracking of an Al–Zn–Mg–(Cu) alloy in humid air. TMS; 2003.
- [56] Thomas RLS, Li DM, Gangloff RR, Scully JR. Metall Mater Trans A 2002;33:1991.

- [57] Nisitani H, Takao K. *Eng Fract Mech* 1981;15:445.
- [58] Louthan Jr MR, Caskey Jr GR, Donovan JA, Rawl Jr DE. *Mater Sci Eng* 1972;10:357.
- [59] Vehoff H. *Microstructures, mechanical properties and processes*. Weinheim, Germany: Wiley-VCH; 2005.
- [60] Lufrano J, Sofronis P. *Acta Mater* 1998;46:1519.
- [61] Warner DH, Curtin WA, Qu S. *Nat Mater* 2007;6:876.
- [62] Qu S, Shastry V, Curtin WA, Miller RE. *Model Simul Mater Sci* 2005;13:1101.
- [63] Warner DH, Curtin WA. *Acta Mater* 2009;57:4267.
- [64] Foiles SM, Baskes MI, Daw MS. *Phys Rev B* 1986;33:7983.
- [65] Daw MS, Baskes MI. *Phys Rev B* 1984;29:6443.
- [66] Angelo JE, Moody NR, Baskes MI. *Model Simul Mater Sc* 1995;3:289.
- [67] Wimmer E. *Solid State Phenomena* 2005;106:168.
- [68] Griffith AA. *Philos Trans Roy Soc Lond A* 1921;221:163.
- [69] Sih GC, Liebowitz H. *Fracture – an advanced treatise*, vol. 2. New York: Academic Press; 1969.
- [70] Mcmeeking RM, Evans AG. *J Am Ceram Soc* 1982;65:242.
- [71] Haftbaradaran H, Song J, Curtin WA, Gao H. *J Power Sources* 2011;196:361.
- [72] Mehrer H. *Diffusion in solids: fundamentals, methods, materials, diffusion-controlled processes*. New York: Springer; 2007. p. 297.
- [73] Sofronis P, Liang Y, Aravas N. *Eur J Mech A – Solid* 2001;20:857.
- [74] Liang Y, Ahn DC, Sofronis P, Dodds RH, Bammann D. *Mech Mater* 2008;40:115.
- [75] Ramasubramaniam A, Itakura M, Ortiz M, Carter EA. *J Mater Res* 2008;23:2757.
- [76] Li DM, Gangloff RP, Scully JR. *Metall Mater Trans A* 2004;35A:849.
- [77] Rose JH, Smith JR, Guinea F, Ferrante J. *Phys Rev B* 1984;29:2963.
- [78] Wipf H, Magerl A, Stump N, Alefeld GB. *Am Phys Soc* 1977;22:440.
- [79] Storms E, Talcottstorms C. *Fusion Technol* 1991;20:246.
- [80] Alefeld G, Volkl J. *Hydrogen in metals I and II*. Heidelberg: Springer; 1978.
- [81] Rice JR. *J Mech Phys Solids* 1992;40:239.
- [82] Wu RQ, Zhong LP, Chen LJ, Freeman AJ. *Phys Rev B* 1996;54:7084.
- [83] Juan YM, Kaxiras E. *Philos Mag A* 1996;74:1367.
- [84] Wu XZ, Wang R, Wang SF. *Appl Surf Sci* 2010;256:3409.
- [85] Fukai Y. *J Alloy Compd* 2003;356:263.
- [86] Fukai Y. *Phys Scripta* 2003;T103:11.
- [87] Suo Z, Shih CF, Varias AG. *Acta Metall Mater* 1993;41:1551.